Enhanced visible-light photocatalysis via back-electron transfer from palladium quantum dots to perylene diimide

Weiqin Wei[a], Zhen Wei[a], Di Liu[b], Yongfa Zhu[a],*

[a] Department of Chemistry, Tsinghua University, Beijing 100084, People's Republic of China
[b] School of Chemical & Environmental Engineering, China University of Mining and Technology, Beijing 100084, People's Republic of China

ARTICLE INFO

ABSTRACT

The electronic-coupling interaction between noble-metal cocatalysts and host semiconductor nanocrystals has been found to be effective for the utilization of the solar energy. However, electron transfer (ET) mechanism between noble metals and self-assemblies has not been elucidated clearly. Here, we revealed a mechanism of back-electron-transfer-enhanced photocatalysis, which contributed to the visible-light photocatalytic improvement of perylene diimide (PDI) assembly for phenolic degradation and hydrogen generation. By compared with the energy level of PDI and Pd quantum dots (QDs), it seemed to be disadvantageous for ET from PDI assembly to Pd QDs, but surface photovoltage spectra showed that this can come true under visible-light irradiation, indicative of formation of a new Schottky barrier resulting from other light-induced transition species. Absorption spectra showed that an additional electronic state existed above the conduction band of PDI assembly originating from PDI radical anions. Such active species provided the light-driven dissipative structure with stable energy and electron flow through two opposite types of ET pathway: one is ET from light-excited PDI anions to Pd QDs and the other is direct electron injection from plasma Pd QDs accumulated with high-energy electrons to PDI neutral molecules. It has been found that continuous ET from PDI assembly to Pd QDs caused the plasma resonance of the Pd QDs to be higher in energy to overcome interfacial energy barrier. And then back-ET from Pd QDs to neutral PDI molecules occurred and led to formation of more PDI radical anions that were important for the improvement of the photocatalytic activity. These findings provide a new strategy for the development of highly efficient visible-light photocatalysts based on self-assembly for energy production.

1. Introduction

Organic semiconductor-based materials have attracted extensive attention for their applications in pharmaceuticals and optoelectronics, such as solar cells [1], optoelectronic devices [2], transistors [3], light-emitting diodes [4], and sensors [5]. Environmental treatment through photocatalytic degradation [6,7], fuel production through light-driven water splitting [8–10] and organic synthesis [11,12] have been achieved using self-assembled supramolecular systems. The photocatalytic performance of self-assembly can be enhanced by introducing functional groups (covalently [13] or noncovalently [14] linked acceptor-donor dyads), integrating acceptor and donor units (C_3N_4-graphene [15] or porphyrin/phthalocyanine-fullerene pairs [16]), and forming short-range π-π stacking structure [17]. Besides, the underlying electronic-coupling interaction of organic semiconductor-based materials plays a crucial role in the adjustment of the conduction band to improve potential redox capability.

Studies of perylene diimide (PDI) have mainly concentrated on the pathway-controlled self-assembly of well-defined structures [18–20] and optoelectronic performances [1,21,22]. PDI can catalyze the reduction of aryl halides [23] and the oxidation of benzyl alcohols and amides [12] due to photoinduced electron transfer (ET). However, the ET efficiency is susceptible to π-π stacking tightness and π-π stacking distance and thus photogenerated electrons may not promptly migrate away before electron-hole recombination. Unlike Frenkel excitons in organic polymers with high exciton-binding energies [24,25], the photoexcitation of PDI assembly generates a PDI radical-anion excited state [26] which possesses high activity. Because of its strong reduction power [23], extensive light absorption [26] and one-dimensional charge-transport promoter [17,27] in photocatalysis, increasing the concentration of the PDI radical anions in PDI assembly is a very effective method to enhance the photocatalytic performance. Electron-hole recombination competes with charge separation and determines the photocatalytic performance of a catalyst. Back-ET is one of the important factors leading to electron-hole recombination [28]. However, if back-ET from an electron-storage material to PDI neutral

molecules enables PDI radical anions, it would be exciting because we could utilize back-ET to improve the photocatalytic activity. Based on the charge-separation capability of Pd metal and the catalytic "memory" effect originating from electron storage [29–31], Pd quantum dots (QDs) were selected as a research subject for this purpose.

PDI is a cocatalyst and sensitizing agent that can utilize solar fuel for hydrogen evolution [32–35]; however, the redox capability of its assembly as a host semiconductor is very weak, compared with inorganic semiconductors. Therefore, the low photocatalytic activity significantly limits its implementation in industrial energy applications. PDI radical anions in the assembly can catalyze hydrogen evolution but only with low contents, which is not enough to meet the harsh hydrogen-production conditions. Therefore, understanding how to tune the energy levels of PDI assembly and modulate interfacial ET ways to acquire high photocatalytic activity is a challenge. In this work, Pd@PDI/P25 and PDI/Pd@P25 architectures where Pd QDs were located inside and outside the PDI assembly were created to enhance the visible-light photocatalytic activity of the PDI assembly. We systematically elucidated the transient ET process between the PDI assembly and Pd QDs, and revealed how the photocatalytic activity of the PDI assembly was enhanced under the self-built electric-field. The back-ET enabled the synergistic action of the plasma Pd metal and the PDI assembly. Through the way, the composite catalyst containing the covered Pd QDs achieved far higher hydrogen yield than PDI/P25. In addition, we revealed the photocatalytic molecular mechanism of photocatalytic phenol oxidation and hydrogen evolution via DFT calculation. This work provides significant guidance and theoretical value for the design of assembly-based composite photocatalysts.

2. Experimental section

General. All chemical reagents were purchased from Sigma-Aldrich and were used without further purification. Distilled water was used in the experiments.

2.1. Preparation of PDI/P25, PDI/SiO₂, Pd@PDI/P25, PDI/Pd@P25 and PDI/Pd@SiO₂

PDI/P25 and PDI/SiO₂ powders were prepared according to the literature [17]. PDI/P25 (1.75 g) powders were suspended in dilute hydrochloric acid (24 mL, 2 M) with ultrasonic dispersion for 2 h and then transferred into teflon-lined autoclave. Then polyvinylpyrrolidone K30 (4.8 g) dissolved in dilute hydrochloric acid (18 mL, 2 M), PdCl₂ (54 mg) dissolved in dilute hydrochloric acid (6 mL, 2 M) and NaI (1.8 g) dissolved in dilute hydrochloric acid (12 mL, 2 M) were added into the dispersion phase of PDI/P25 successively. The mixture in teflon-lined autoclave was heated at 170–180 °C for 2 h, followed by natural cooling, centrifugation and washing with dilute hydrochloric acid. The mixture was freeze-dried under vacuum for 24 h to give Pd@PDI/P25 (H-2 represented Pd@PDI/P25 with Pd mass ratio of 0.02 with respect to the mass of P25). The other H series catalysts were prepared by the same method. Pd@P25 was prepared via the method above. And then PDI/Pd@P25 was prepared by the method same as PDI/P25. PDI/Pd@SiO₂ was prepared similar with PDI/Pd@P25.

2.2. Preparation of Pd nanoparticles

Pd nanoparticles were prepared as following: PdCl₂ (90 mg) and PVP (5 g) was dissolved in 78 mL distilled water. NaI (3 g) in 52 mL distilled water was added into the solution above dropwise. After mixing, the mixture in teflon-lined autoclave was heated at 170–180 °C for 2 h, followed by natural cooling, centrifugation and washing with distilled water and alcohol. The mixture was dried in the N₂ gas flow at the room temperature to give black powder.

2.3. Characterization

TEM was conducted on a JEM 1010 electron microscope at an accelerating voltage of 100 kV. HRTEM and EDS mapping images were taken on a JEM 2100F electron microscope at an accelerating voltage of 200 kV. Absorption spectra were recorded with a Hitachi U-3900 spectrophotometer. PL spectra were performed on an F-7000 FL spectrometer with excited wavelength of 550 nm. FTIR spectra were obtained with a Bruker VERTEX 700 spectrometer. Fluorescence spectra were carried out with a QY-2000 fluorescence spectrometer. XPS was measured using a PHI quantro SXM spectrometer. Electrochemical measurements were performed on a CHI660D electrochemical workstation with a three-electrode system in which platinum wire was used as a counter electrode and standard calomel electrode as a reference electrode. Na_2SO_4 ($0.1 \, mol \, L^{-1}$) solution was used as electrolyte. Size distribution was measured by a Horiba SZ-100 Nano Particle analyzer. HPLC was performed on a LC-20AT chromatograph. GCMS was performed on TRACE 1300 gas chromatograph with ITQ 900 MS detector. Surface photovoltage spectra were measured with Omni-λ 3005, model SR540 chopper controller and model SR830 DSP lock-in amplifier. ESR spectra were recorded on a JES-FA200 ESR spectrometer at room temperature. Fluorescence stability test was conducted with Nanolog FL3-2iHR infrared fluorescence spectrometer. XRD pattern was recorded with a Bruker D8 advance diffractometer.

2.4. Photocatalytic activity measurements

The photocatalytic activities of the catalysts were evaluated by the decomposition of MO ($2 \times 10^{-5} \, mol \, L^{-1}$), phenolic compounds (5 ppm) with visible light (λ > 420 nm). The photodegradation reactions were carried out with aqueous solution (50 mL) containing HCl (1.2 M) and photocatalysts (20 mg). Reaction mixture was stirred in the dark to reach adsorption−desorption equilibrium. After 1 h, the mixtures were stirred under the irradiation with a 500 W xenon lamp containing 420 nm cut-off filter or with a 300 W high pressure Hg lamp containing 365 nm cut-off filter. Samples (3 mL) were collected at certain time intervals followed by centrifugation to remove the precipitation in reaction mixtures. A Hitachi U-3010 UV–vis spectra photometer was used to measure the maximum absorption of MO at 506 nm. HPLC was conducted to measure the peak area of phenol at 270 nm (C18, 150 mm × 4.6 mm × 5 μm, $1 \, mL \, min^{-1}$, H_2O/MeOH = 45/55). Trapping active species experiments were carried out using 1,2-benzoquinone as superoxide radical scavenger, KI as hole scavenger, and isopropyl alcohol as hydroxyl radical scavenger. Concentration or volume of the reagents above was as follows: 1,2-benzoquinone ($1 \, mmol \, L^{-1}$); KI ($1 \, mmol \, L^{-1}$); isopropyl alcohol (4.8 μL).

H₂ generation experiments were carried out in a top-irradiation type reactor connected to a closed gas circulation and evacuation system (CEAULICHT, Beijing). Photocatalyst powder (30 mg) was suspended with ultrasonic dispersion in 100 mL aqueous solution containing HCl ($1.1 \, mol \, L^{-1}$) and anhydrous Na_2SO_3 (2.5 g) as sacrificial agent to consume holes. Before visible-light irradiation, small amount of (hydro) chloroplatinic acid was added and the system was evacuated. The system was pre-irradiated for 0.5 h under continuous vacuum extraction. (400 W Xenon lamp, with 420 nm cut-off filter, 17 A current) The reaction temperature was maintained at 6 °C during the experiment. H₂ amount was detected by gas chromatography with N₂ as carrier gas.

2.5. Density functional calculations

DFT calculations were exhibited by Gaussian 09 and Gauss View 5.08 with the B3LYP hybrid DFT exchange-correlation function. The standard Gaussian basis function 6-31 + G** was used for the calculation.
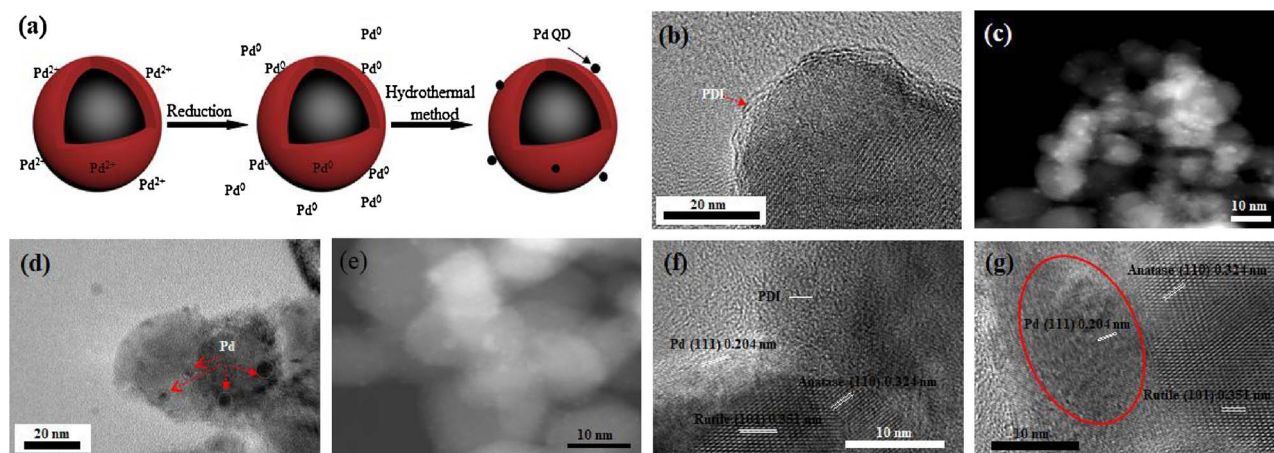
Fig. 1. (a) Schematic illustration of the synthetic process. (b) HRTEM image of PDI/P25. (c) High-angle annular dark field (HAADF)-STEM image of H-2. (d) HRTEM image of H-2. (e) HAADF-STEM image of P-2. HRTEM image of (f) H-2 and (g) P-2. Pd@PDI/P25 and PDI/Pd@P25 are named H-n and P-n, respectively. ("n" represents the theoretical weight ratio of Pd vs. P25).

3. Results and discussion

3.1. Morphology of the catalyst

Pd QDs were incorporated into catalysts via hydrothermal reduction method [36] to fabricate exposed and covered Pd QDs as shown in Fig. S1. The PDI structure was not destroyed during the hydrothermal process (Fig. S2), and the phase ratios of anatase and rutile for all the catalysts were verified to be approximate by comparing the area ratios of the diffraction peaks in X-ray diffraction. (Table S1) As can be seen from Fig. 1b, PDI/P25 core-shell structure was observed, which consisted of TiO_2 core and PDI assembly shell (5–10 nm), as presented in our preliminary work [17]. According to the preparation method of Pd QDs reported [36], we chose the temperature 180 °C and hydrothermal time 2 h as the optimum conditions. In the formation process of the Pd QDs (Fig. 1a), it involved the pre-adsorption of Pd^{2+}, reduction to Pd° and hydrothermal crystallization. To prepare the P series in which Pd QDs were covered by PDI assembly, we loaded the Pd QDs on TiO_2 nanoparticle first followed by the PDI assembly covering. Size distribution in the process was measured to verify the combination as shown in Fig. S3. As presented in transmission electron microscopy (TEM) image, (Fig. 1d) the Pd QDs on the H-type catalyst were randomly distributed around the catalysts, with an average diameter of ∼2 nm. The dark field TEM images (Fig. 1c, e) and energy dispersive spectroscopy mapping (Fig. S4) also confirmed a uniformed distribution of the Pd QDs over the whole TiO_2 nanoparticle. Furthermore, Pd 3d peaks at 340.7 and 335.6 eV which were detected by X-ray photoelectron spectroscopy (Fig. S5) revealed the metallic nature of the Pd QDs. To demonstrate that these two types of catalysts had internal and external distribution of the Pd QDs, the relative location between Pd QDs, TiO_2 nanoparticle and PDI assembly was confirmed via high-resolution TEM (HRTEM). The corresponding lattice fringes of 0.204 nm, 0.324 nm and 0.351 nm can be ascribed to the (111) plane of Pd QD, the (110) plane of anatase and the (101) plane of rutile, respectively. In Fig. 1f, the bulk of the Pd QD in the H series was apparently exposed outside the PDI assembly, while the Pd QDs of the P series were covered by the PDI assembly layer (Figs. 1g, S6). Furthermore, the chemical depth profiling analysis has been performed. Fig. S7 showed that Ti amount of P and H series both increased with an increase of detection depth. However, a notable decrease in Pd amount of the H series and a small increase in Pd amount of the P series were observed, respectively, indicating the successful formation of the exposed and covered Pd QDs. Inductively coupled plasma atomic emission spectroscopy showed the Pd and Ti weight percentages of the P and H series were nearly the same (Table S2).

3.2. Electron transfer dynamics

The dipolar field interactions of the Pd QDs [37] and the effective orbital overlap between perylene and Pd, [38] as evidenced by the red-shift of C=O band at $1691\,cm^{-1}$ and perylene ring stretches at $1596\,cm^{-1}$ when PDI interacted with Pd QDs (Fig. S3), lay a foundation for the electronic coupling between PDI and Pd QDs. Moreover, the Fermi level of PDI (−4.5 eV versus vacuum level) [39] is higher than that of Pd nanoparticle (∼ −5.2 eV) [40]. Therefore, such energy level difference would form upward-bent energy band in the vicinity of PDI assembly surface and is actually disadvantageous for the ET from PDI to Pd QD due to formation of electron depletion region in the interfacial state of the PDI assembly [41]. However, the frontier orbital of PDI radical anions (LUMO: −5.72 eV versus NHE) could make the ET from PDI assembly to Pd QDs thermodynamics feasibility. Time-resolved diffuse-reflectance spectroscopy excited at 464 nm was performed to provide direct evidence of the ET from PDI assembly to Pd QDs. The transient fluorescence trace (Fig. 2a) was fitted to a single exponential function to acquire fluorescence lifetimes of P-1 (1.083 ns), P-2 (1.298 ns), H-2 (0.693 ns) and H-4 (0.768 ns). Compared with PDI/P25 [17], the shorter fluorescence lifetime indicated nonradiative energy transfer to the Pd QDs. For various P and H series, the decay rate of fluorescence species performed the distinction. It was noted that the fluorescence lifetimes of P-2 was two times longer than that of H-2. Such a distinction correlated with the less recombination of electrons and holes. Photoluminescence spectroscopy was also employed to evaluate the photogenerated ET (Fig. 2b). Under the excitation of a 550-nm laser, PDI/P25 exhibited strong luminescence intensity at 703 nm. It can be seen that the Pd-loaded catalysts showed little change in the absorption intensity, but the luminescence intensity of PDI was decreased by 72.5%. For the Pd-loaded catalysts, PDI molecules still acted as luminescence centers and mainly performed the radiation luminescence from the recombination of electron-hole pairs. However, the free electrons transferred from PDI assembly to Pd QDs were quenched via a nonradiation recombination, which significantly declined the probability of radiative transition. Another evidence was red-shift of PDI fluorescence emission (Fig. S8), indicative of narrower band gap. Some transition species of PDI were formed under light excitation [23,26]. It was calculated that PDI^+ or PDI^- had a lower energy level gap than PDI [17]. So it was reasonable to speculate that more PDI molecules can be transformed into PDI^+ or PDI^- via the ET between PDI assembly and Pd QDs. These results proved that the Pd QDs can harvest photogenerated electrons excited in the PDI assembly.

The catalytic activity of a semiconductor photocatalyst is largely related to the charge-transport behavior of the surface or interface of a
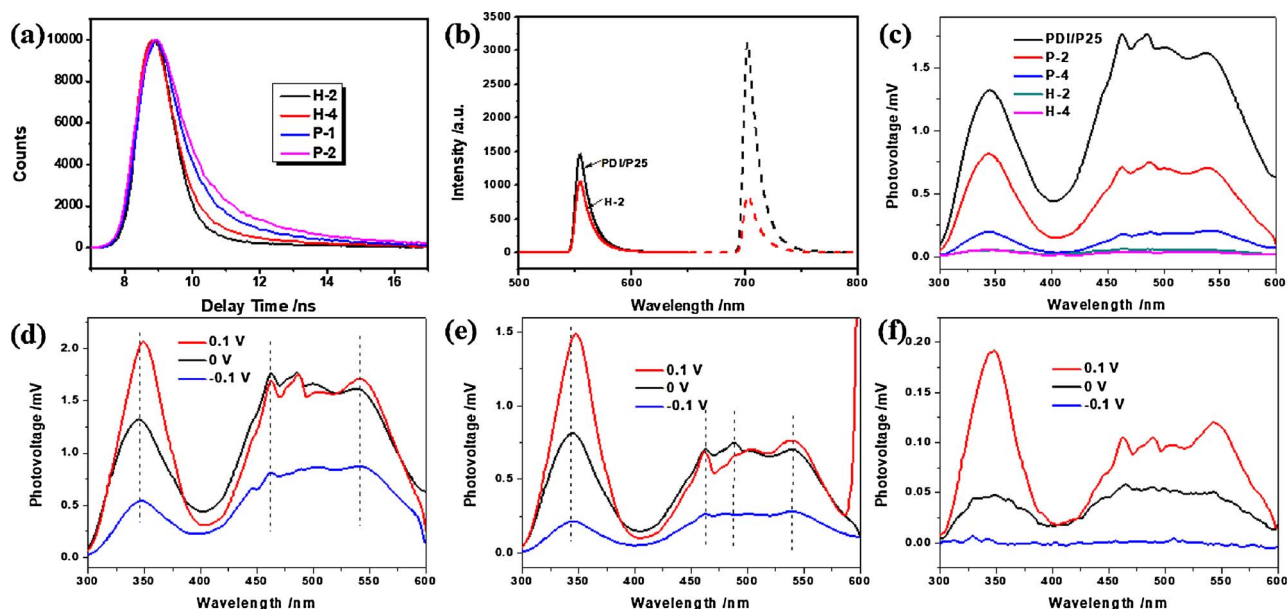
Fig. 2. (a) Transient absorption spectra of P and H series excited at 464 nm. (b) Solid photoluminescence spectra of H-2 and PDI/P25. The solid line referred to excitation and the dashed line referred to emission. (c) Surface photovoltage spectra of H-2, H-4, P-2, P-4 and PDI/P25. Electric-field-induced surface photovoltage spectra of (d) PDI/P25, (e) P-2 and (f) H-2 at the voltage bias of −0.1 V, 0 V and 0.1 V.

material. Therefore, the surface photovoltage (SPV) spectroscopy was used to study the effects of the loaded noble metal on the charge-transport behavior of the semiconductor material. SPV spectrum was measured via solid-junction photovoltaic cell of the sandwich structure (indium tin oxide/sample/indium tin oxide). The wavelength between 400 and 600 nm belonged to the absorption region of PDI. Pd was found to have no surface photovoltage (Fig. S9). Before illumination, the contact between PDI assembly and Pd QDs made the surface energy band of the PDI assembly upward-bent as mentioned above. In Fig. 2c, it can be seen that the surface photovoltage toward PDI/P25 was positive in the region, indicating that PDI assembly was a n-type semiconductor and photoinduced holes moved toward the irradiation side. As compared to the Pd-loaded catalysts, the SPV response was significantly lower than that of PDI/P25, suggesting the Pd QDs can affect the separation of photoinduced carriers and lower the surface barrier of the PDI assembly [41]. Intriguingly, the surface voltages toward H-2 and H-4 were far less than the surface voltage toward PDI/P25. It was inferred that by loading the Pd QDs, the equilibrium interfacial state density of the PDI assembly were nearly consistent before and after illumination; however, to overcome interfacial electrostatic potential and realize the ET from PDI assembly to Pd QDs, a new downward-bent Schottky barrier must be formed. In the term of thermodynamics, ΔG of the charge-redistribution underwent a tiny change before and after illumination due to the consistent interfacial state density. Assuming ΔS was not changed in the solid system, the enthalpy caused by the absorption of a mass of incident photons need to be rapidly transferred to the Pd QDs via charge injection and converted into plasma oscillation energy of the Pd QDs. Else, the difference of the SPVs between P and H series was due to the distribution of the Pd QDs inside and outside the PDI assembly shell, corresponding to different morphologies. Importantly, the particular surface energy level also implied two reverse types of ET pathway between PDI assembly and Pd QDs. (For detail, see the SI, Fig. S10) To further examine the transfer of photoinduced charge carriers, electric-field-induced SPVs were measured. Fig. 2d, 2e showed that at a negative voltage bias, the surface voltage was declined. It suggested the negative external electric field enabled photoinduced electrons to migrate from the surface to the bulk, so that electric energy band in the vicinity of the PDI assembly surface was down-shifted [41]. But positive voltage bias could not accelerate electrons to accumulate on the surface of PDI assembly, possibly because too many electrons

existing on the surface of PDI assembly promoted the combination of electrons and holes. But for H series, due to the existing of the Pd QDs on the surface of PDI assembly, it could be observed that positive voltage bias enhanced SPV intensity, (Fig. 2f) suggesting positive external electric field promoted photoinduced ET from PDI assembly to Pd QDs.

The wavelength between 300 and 400 nm corresponded to the absorption region of TiO₂. Pd QDs promoted ET and energy transfer from TiO₂ to Pd QDs only under UV light rather than under visible light. In our study, visible-light performance was only concerned and thus light-excited TiO₂ did not exist in the visible-light photocatalysis. It is known that visible-light excited electrons of PDI could transfer to TiO₂ [17]. After that, a part of the electrons in TiO₂ transferred into Pd QDs, because as seen from the UV-light region, it was due to ET from TiO₂ to Pd QDs leading to a decrease of SPV. Undoubtedly, the downward-bent surface energy band between TiO₂ and Pd QDs was formed because TiO₂ has a higher Fermi lever than Pd QDs. (Fig. S10) It suggested feasible ET process from TiO₂ to Pd QDs but adverse ET process from Pd QDs to TiO₂, that is, the electrons accumulated in the Pd QDs from PDI would require higher energy to transfer to TiO₂ than to PDI assembly. The ET route to PDI was the preference because the upward-bent Shottchy barrier existed in the interface between PDI and Pd. It was also found that when the external voltage of +0.1 was applied, the SPV peak toward TiO₂ was red-shift by 5 nm, signifying the characteristic of bound exciton. For PDI assembly, the SPV peaks were unchanged, corresponding to the characteristic of free exciton. The free excitons in the PDI assembly could diffuse farther and thus enable more efficient ET from PDI to Pd QDs [42,43].

3.3. Back-electron transfer dynamics

To illustrate back-ET from Pd QDs to PDI, it is necessary to detect PDI radical anions of the P and H series. An isolated PDI molecule has difficulty transforming into a stable PDI anion without the assistance of reduction agent due to intermolecular ET and quenching [23]. In PDI assembly, the effective in-plane electron delocalization over the whole PDI skeleton leaves the PDI anion away from the recombination center and results in a stable state in the assembly [20,26,27,43]. Therefore, absorption spectroscopy can be employed to detect the PDI radical anions. The absorption bands of the PDI assembly at 498 and 550 nm are attributed to the electronic transition in the isolated molecule and
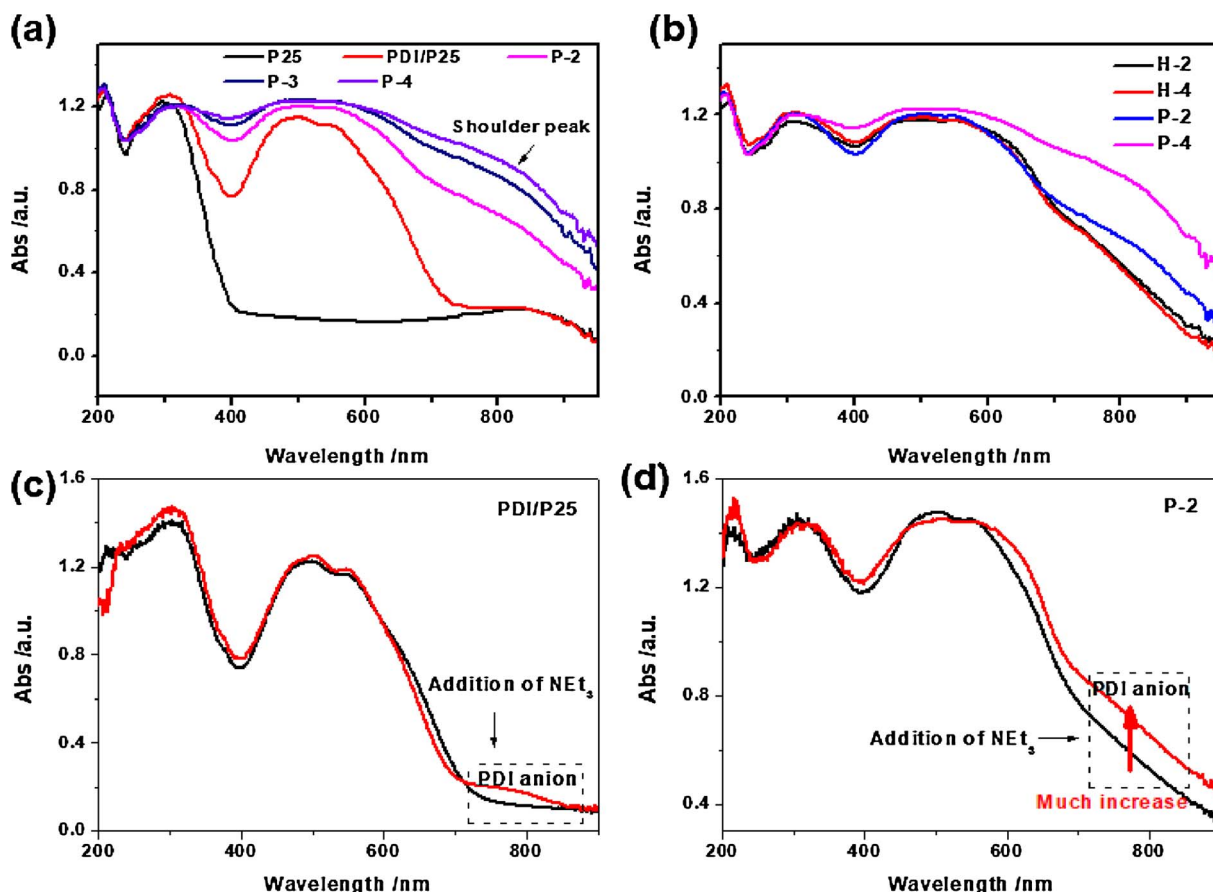
Fig. 3. UV–vis diffuse reflection spectra of (a) the P series and (b) comparison of the P series and H series. Change in the absorption spectra of (c) PDI/P25 and (d) P-2 upon successive addition of NEt$_3$. The red line corresponded to the sample of adding NEt$_3$.

the π-electron delocalization between PDI chromophores, respectively [44,45]. The corresponding bands were also observed in the spectra of the P and H series. (Fig. 3a,b) Interestingly, the Pd-loaded catalysts showed a "shoulder" absorption between 700 and 850 nm. Meanwhile the P series presented the more obvious "shoulder" absorption than the H series under the same Pd amount, indicating that absorption band cannot be attributed to plasma reasonance. For P series, the amount of Pd QDs determined the intensity of the "shoulder" band, but for H series, the intensity of the "shoulder" band did not change with the amount of Pd QDs. It has been reported that the PDI radical anions have three feature absorption peaks at 700, 790 and 950 nm [26]. The feature peaks of PDI neutral molecule and PDI radical anion could change upon exposure to electron donors, such as amines [23,42,43]. Therefore, to confirm the "shoulder" peak between 700 and 850 nm was attributed to a electronic transition of PDI radical anion, NEt$_3$ can be used to detect the growth of the feature peaks. Fig. 3c showed that after adding NEt$_3$, the absorption peak of PDI/P25 at around 790 nm emerged, suggesting NEt$_3$ promoted more PDI radical anions [42,43]. Similarly, the absorption of P-2 at around 790 nm was enhanced significantly (Fig. 3d). Therefore, it was comfirmed that the 'shoulder' peak at around 790 nm was due to PDI radical anions. To simplify the research system and eliminate the interaction between Pd QDs and TiO$_2$, SiO$_2$ was chosen as the substrate to prepare PDI/Pd@SiO$_2$ which included ~2% Pd and ~8% PDI through the same method. Fig. S11 showed the Pd-loaded PDI-SiO$_2$ series and the composite series with the other PDI assembly have more significant 'tail-like' feature at 700–850 nm than at the other wavelength, indicative of formation of the transition species.

Electron spin resonance (ESR) spectroscopy as a sensitive, specific method for studying unpaired electrons, was widely used in many branches of science [46–49]. Here, it was employed to provide evidence to confirm the existence of high-energy electrons accumulated in the Pd QDs. The g factor and peak-to-peak ESR linewidth, ΔH_{pp}, were measured to be: a) PDI/P25, g = 2.0009, ΔH_{pp} = 0.40 mT; b) P-2, g = 2.0010, ΔH_{pp} = 0.40 mT; c) H-2, g = 2.0006, ΔH_{pp} = 0.84 mT. Due to limited penetration power of microwave, the ESR signals toward TiO$_2$ core and Pd QDs of P-2 cannot be detected. Hence, the ESR signs toward PDI/P25 and P-2 arise from the delocalization electrons in PDI assembly and the ESR signs toward H-2 come from the delocalization electrons in the PDI assembly and electrons in the Pd QDs, which were all smaller than free electrons ESR g value (2.0023). It has been reported that metallic Pd nanoparticles have a weak, susceptible ESR signal [50]. However, it was worth noting that the ESR intensity of H-2 was significantly greater than that of PDI/P25 and P-2, (Fig. S12a) indicating more paramagnetic centers induced by electron injection from excited PDI. Moreover, the signal toward H-2 was enhanced over time under the irradiation and then was slowly reduced when the light was shut off, (Fig. 4a) which indicated photogenerated electrons flowed into the Pd QDs and were accumulated in the Pd QDs [51]. For PDI/P25, a negligible change was showed in this case. (Fig. S12b) As we know, when a pool of the incident light shines on metal surface, the collective resonance of the electrons in metal occurs. In our systems, the ET from PDI assembly to Pd QDs enhanced the plasma resonance effect, and consequently, more electrons with higher energy were formed, which resulted in the enhanced ESR signal toward H-2. In addition, we can infer that the electrons accumulated in the Pd QDs had a lifetime longer than 10 μs, because the unpaired electrons with short lifetime less than 10 μs cannot be detected by the present ESR instruments.

To further verify the high-energy electrons in the Pd QDs, the energy of the electrons accumulated in the Pd QDs should be determined
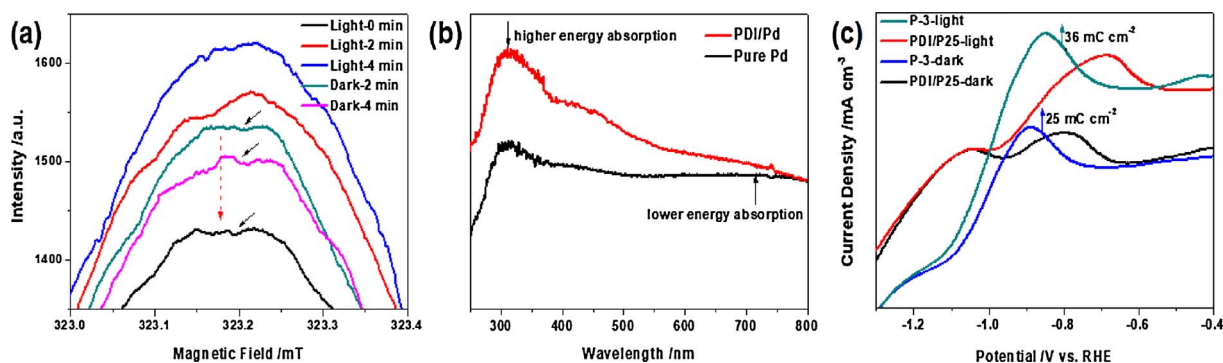
Fig. 4. (a) ESR spectra of H-2 under the visible-light irradiation. (λ > 420 nm) The samples were irradiated for 2 and 4 min and then remained in the dark for 2 and 4 min. (b) Absorption spectra of 8% PDI/Pd core-shell structure and pure Pd nanoparticles. (c) Cyclic voltammetry (CV) curves of PDI/P25 and P-3 in 0.1 M Na_2SO_4 solution with a scan rate of 100 mV s^{-1} and irradiation visible light of more than 420 nm. Compared with PDI/P25, total charge transferred during the reduction process of P-3 was increased by around 25 and 36 mC cm^{-2}, respectively, in the dark and under the illumination.

by variations of its plasma frequency using UV–vis absorption spectroscopy. It has been well-documented that the plasma resonance band of plasma metallic Au can be detected via UV–vis absorption spectra [52,53]. The plasmon resonance band of pure Pd nanoparticles was found to be a broad band, (Fig. 4b) which has been found by Xia et al. [54]. For the PDI-Pd-P25 system, it's difficult to observe the maximum plasma resonance band of the Pd QDs due to overlapping with the PDI bands. Here, we realized the band relative intensity of PDI and Pd changed with different amount ratio of PDI and Pd. Hence, PDI/Pd (W_{PDI}/W_{Pd} = 8%) consisting of PDI shell and Pd core was prepared. By the way, we can significantly decrease the absorbance of the PDI assembly and effectively reduce its interference toward the Pd resonance band. The morphology of PDI/Pd was shown in Fig. S13. Interestingly, the Pd resonance absorption of PDI/Pd at 308 nm (Frequency = 9.7 $*10^{14}$ s^{-1}) was enhanced significantly compared with pure Pd nanoparticles, (Fig. 4b) which indicative of the enhanced Pd plasma resonance and a larger proportion of the high-energy electrons than pure Pd. These electrons had higher energy to overcome the interfacial barrier. The band at 308 nm was not attributed to polyvinyl pyrrolidone as shown in Fig. S14. In conjunction with the results above, this phenomenon clearly suggested more high-energy electrons in plasma Pd metal were formed via the ET from the PDI assembly and the electron accumulation in the Pd nanoparticles.

A series of electronchemical experiments were designed based on the literature [55] to gain more insight of Pd plasma resonance effect to the ET from Pd QDs to PDI assembly. As shown in chronoamperometric I-t curve under visible-light illumination, (Fig. S15) P-3 and H-3 exhibited prompt current responses to the on-off illumination cycles. Due to the electron accumulation in the Pd QDs, it presented the discharge effect in the dark. Moreover, the overpotential corresponding to the current density of 10 mA cm^{-2}, a metric related to solar fuel systhesis, was obviously decreased from 555 to 378 mV, (Table S3) close to the value of benchmark of IrO$_2$ catalysts. The results suggested the necessity of the Pd QDs for the enhancement of photoelectrical conversion efficiency. Importantly, under visible-light illumination, the Tafel slope of P-4 was significantly decreased by 30 mV dec^{-1}, compared with that in the dark. (Fig. S16) It should be noted that PDI amount was 4 times higher than Pd amount which was less than 3%. This clearly demonstrated the ET kinetics over the system was facilitated by the irradiation-induced Pd plasma resonance. As to PDI-based photocatalysts, the radical reaction generally involved the reduction of PDI to PDI- [23,56]. (Scheme S1) Then the highly reduction PDI^{-*} were believed to enable the hydrogen evolution and pollutant degradation under the visible-light illumination. Herein, the redox behavior of PDI-/PDI was investigated via cyclic voltammetry (CV) method at room temperature. In Fig. 4c, the reduction peak of PDI into PDI- was clearly showed at ca. −1.2 V. When the P-3 electrode was irradiated (λ > 420 nm), the reduction peak of PDI was shifted by 0.184 V with respective to PDI/P25,

larger than the difference in the dark. The result may possibly involve in the formation of the interfacial intermediate states. Clearly, the current density of PDI-/PDI of P-3 was indeed enhanced under the irradiation. According to the method reported [55,57], the extent of the PDI-/PDI transformation was qualitatively measured by intergrating the reduction peak. (Table S4) Strikingly, under the irradiation, the reduction extent of PDI- of P-3 was increased by 45% as compared to P-3-dark, larger than the difference of PDI/P25. It indicated that electrons accumulated in the Pd QDs were driven flowing into the PDI assembly. Meanwhile, another evidence came from CV cycle experiment. After five times cycling, the reduction peak area of P-4 was reduced significantly, while PDI/P25 showed no change. (Fig. S17) This suggested the existence of the Pd QDs was critically important for the improvement of PDI- formation. Additionally, the electron released rate from Pd QDs to PDI assembly was indeed slow to lead to the fluorescence stability. (Fig. S18) The slow electron released process from Pd QDs to PDI assembly reduced the quenching of the PDI radical anions and cations in the PDI assembly, which was one of the conditions for the formation of more active PDI radical anions. Therefore, it could be concluded that the plasmonic excitation of Pd QDs enhanced the reduction of PDI into PDI- in PDI-Pd photocatalysts. In total, the results above forcefully proved that the ET from PDI assembly to Pd QDs left a population of high-energy electrons in the Pd QDs, and the direct electron injection from Pd QDs into PDI assembly formed more PDI radical anions.

3.4. Enhanced visible-light photocatalytic activity

The Pd-loaded catalysts exhibited more excellent visible-light photocatalytic activity for the degradation of methyl orange (Fig. 5a) and phenol (Fig. 5b) in comparison to PDI/P25. The photocatalytic degradation was carried out in acid solution to prevent the disaggregation of PDI. For the H series, the rate constant k increased when the Pd amount increased from 1% to 4% due to dangling bonds of exposed Pd QDs. For the P series, at a ratio of ~2%, the value of the rate constant reached an optimum value, suggesting P-2 performed the highest activity. However, with a continuous increase in Pd amount, the rate constant decreased, suggesting Pd amount was not the determining factor, but the photocatalytic activity of the P series was mainly dependent on the PDI assembly. PDI radical anions contributed to photocatalytic reaction. As mentioned above, the electrons in plasma Pd QDs would tend to back-transfer into PDI assembly thus increasing active species on the PDI assembly. Although increasing Pd amount would be in favor of formation of PDI anions, too many electrons accumulated in the PDI assembly would easily result in the combination of electrons and holes, which resulted in decrease of the reaction rate constant after ~2% Pd amount. Additionally, PDI/Pd also exhibited excellent photocatalytic dye degradation activity, approaching to P-2, while the activity of the mechanical mixture was reduced half. (Fig.
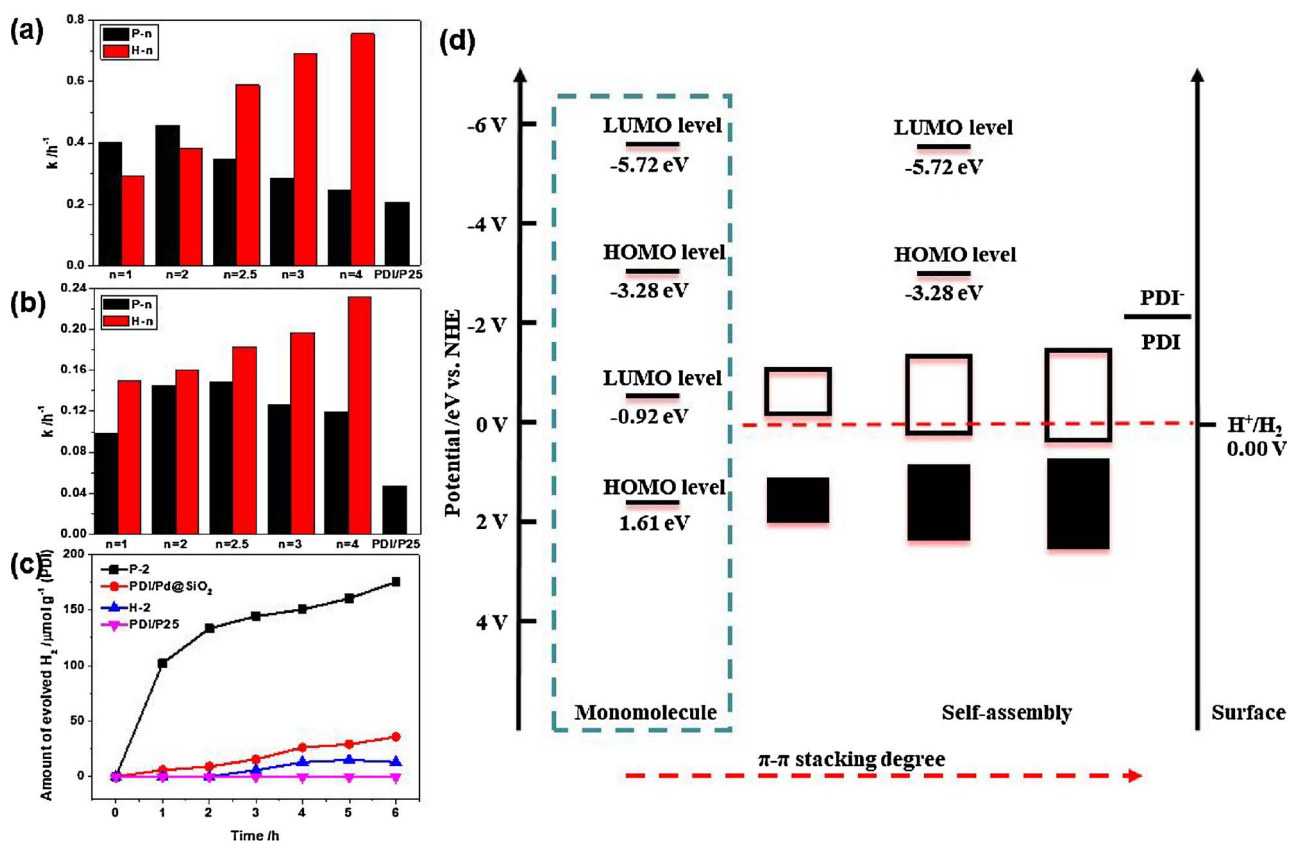
Fig. 5. Photocatalytic degradation of (a) methyl orange and (b) phenol. (c) Photocatalytic hydrogen evolution ($\lambda > 420$ nm). (d) Photocatalysis mechanism of the PDI assembly under the assistant of the Pd QDs.

S19) Isothermal N_2 adsorption and desorption showed that PDI/P25 and Pd-loaded catalysts had the approximate specific surface area. (Fig. S20)

Importantly, it's surprising to find that hydrogen production over the P series was more efficient than PDI/P25 and the H series. (Fig. 5c) P-2 had a much faster rate of hydrogen evolution than PDI/P25. But the activity of hydrogen evolution over P-2 trended to decrease over time possibly because the Pd QDs adsorbed H^+, which would inhibit the back-ET from Pd QDs to PDI assembly. H-2 exhibited excellent photocatalytic degradation, but was found to give a low hydrogen yield. The activity difference between P-2 and H-2 may be because: as shown in Fig. S21, due to the contact between Pd QDs and TiO_2, the ET along the direction from PDI assembly to TiO_2 and then to Pd QDs took place and was more advantageous for the electron accumulation in the Pd QDs enhancing the Pd plasma resonance. As shown in Fig. 5d, for the PDI assembly, a band-like energy-level structure was formed [6,59], suggesting the reduced capability of the conduction band of the PDI assembly inhibated ET from the PDI assembly to the P25 conduction band and hydrogen production. However, the formed PDI radical anions did not take part in the band-like energy-level structure due to their high electronic energy level that did not match with energy level of the neutral PDI molecules, indicating that the electrons of the PDI radical anions existed in nonbonding-type orbitals. Therefore, the PDI radical anions had stronger reduction power for hydrogen evolution.

To reveal the photocatalytic mechanism of the Pd-loaded catalysts, intermediates during the degradation were studied by high performance liquid chromatography. (Fig. S22) By comparison with the chromatograms of the pure substances, the main intermediates were found to be catechol and benzoquinone, which were also evidenced by mass spectrometry. (Fig. S23) To verify the reactive oxidative species (ROS) in the photocatalytic degradation, the active radical-capturing experiment (Fig. S24a) and ESR (Fig. S24b) was performed, revealing

superoxide radicals and holes as the ROS.

Due to π-π interaction, phenol molecules were first adsorbed on perylene unit. It has been known that light excitation of catalyst realized the photoadsorption of oxygen [60]. Charge separation in the PDI assembly also enabled the chemical adsorption of singlet O_2 (1, Fig. S25a). Through DFT calculations, we found that the HOMO level (-7.298 eV) of singlet O_2 matched well with the LUMO level (-7.272 eV) of PDI^+, which suggested the $(\pi^*_{2p})^2$ electrons in the HOMO level of singlet O_2 can be delivered to the LUMO level of PDI^+, but the LUMO level (-8.818 eV) of triplet O_2 did not match well. To enhance the energy-level matching of O_2 with PDI^+, the energy transfer between PDI* and triplet O_2 was crucial to form singlet O_2 via the collision. The collision would transfer the excited energy of 2.542 eV (the energy level gap of PDI) to triplet O_2 to fulfill the energy difference (1.674 eV) of the transformation from triplet O_2 to singlet O_2. To confirm the binding site of singlet O_2 in PDI, the Mulliken charge distributions of PDI, PDI^+ and PDI^- were obtained via DFT calculations. From Fig. 6a, b, in the transformation from PDI to PDI^+, the charge of the carbon atom in the marked circle region increased by 0.024, the largest charge change among all carbons with positive Mulliken charges. Xu group has revealed carbon atoms could become the active sites for water splitting [61]. Dissolved oxygen was selectively absorbed by the carbon atom with less Gibbs energy change. Singlet O_2 acted as an electron donor and undoubtedly tended to interact with positive atom because of forming a more stable intermediate state. Moreover, the effective electron cloud overlap of singlet O_2 and PDI^+ formed in this region (Fig. 6e, f) and one electron of singlet O_2 was given to PDI^+. ET along the π-π stacking direction transferred two electrons to the π^*_{2p} orbital of the surface-bound $O_2 \cdot ^+$ and then generated a surface-bound $O_2 \cdot ^-$, similar with the formation of surface $O_2 \cdot ^-$ in BiOCl with oxygen vacancies [53]. ET to the surface-bound $O_2 \cdot ^+$ occurred mainly through the action of $C_{0.06}$-$C_{0.038}$-$C_{0.06}$ where negative charge of PDI^- was

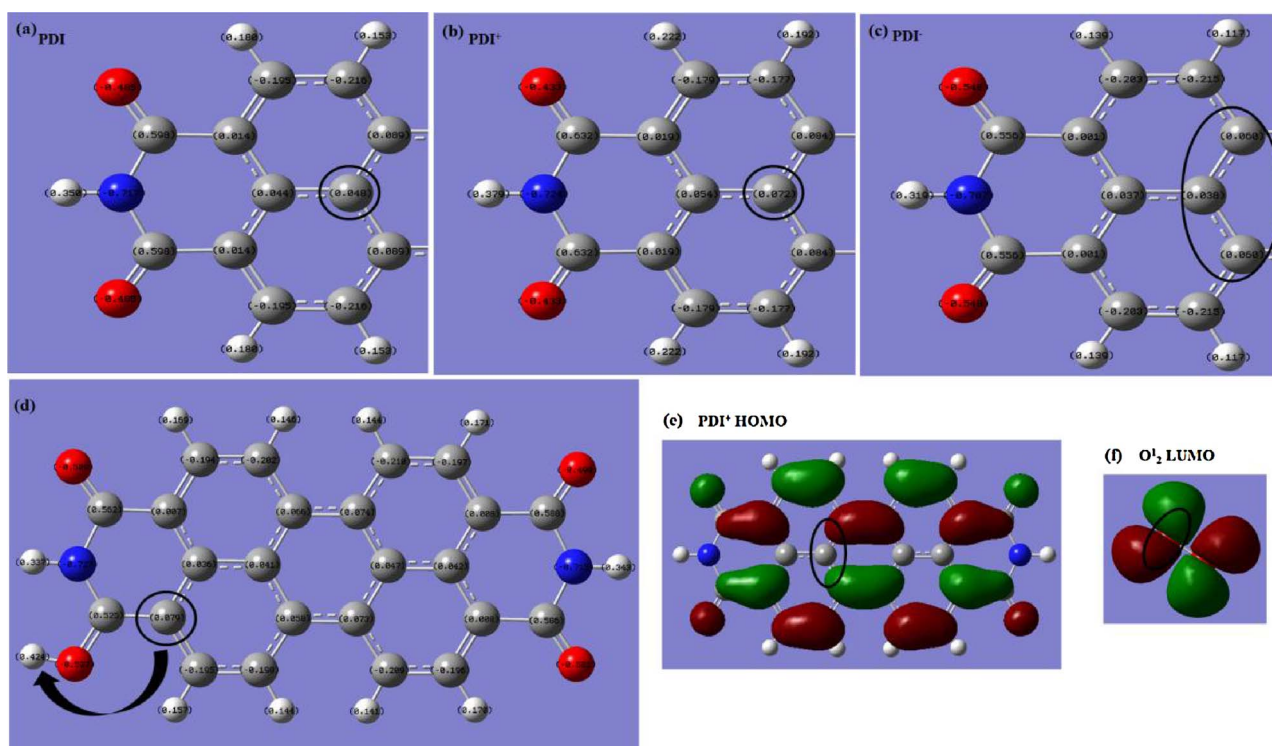**Fig. 6.** Mulliken charge distribution of (a) PDI, (b) PDI$^+$, (c) PDI$^-$ and (d) PDI binding with H$^+$ in C=O. (e) Optimized HOMO level of PDI$^+$. (f) Optimized LUMO level of singlet O$_2$.

concentrated. (Fig. 6c) Due to electron accumulation in the Pd QDs, the plasmonic oscillation of the Pd QDs was enhanced significantly, which led to the direct electron injection from Pd QDs to PDI assembly, like the behaviors of plasma Au [58]. The polar structure adsorbed the surface-bound O$_2$·$^+$ ensured the directional migration of "hot electrons" into surface-bound O$_2$·$^+$. Hence, electron transport along π-π stacking direction in the PDI assembly promoted the activation of O$_2$ to surface-bound O$_2$·$^-$. (2, Fig. S25a) With the help of h-O$_{(1)}$-O$_{(2)}$, unstable cyclic peroxide was formed [62,63] to enable consequent cleavage carbon-carbon bond. In the entire degradation, four h−O−O$^-$ active species were consumed along with the generation of H$_2$O$_2$ in acid solution [64]. During the photocatalytic degradation, phenol exhaustive oxidation occurred on PDI. (3, Fig. S25a) Theoretical calculation of the phenol degradation pathway was used to analyze how the superoxide radical interacts with the phenol molecule in the ortho position to form cyclic transition states. (Fig. S26) For the hydrogen evolution, as reported that carbonyl group would accept one H atom to form hydrogen bond [20], H$^+$ also bonded to C=O forming C=O−H (Fig. S25b). The edge-to-edge distance in the transversal direction was 1.97 Å [6], and the length of C=O−H was calculated to be 2.32 Å via DFT calculation. Due to the collision of the H atoms between two C=O−H groups of adjacent PDI molecules, an H−H bond (0.75 Å) formed via electron hopping to H$^+$ along with rapid hole consumption by SO$_3$$^{2-}$. The C$_{0.079}$ position where negative charges in such structure were concentrated captured delocalization electrons and delivered the electrons to H of C=O−H. (Fig. 6d) We can exclude the reaction of two H atoms along the π-π stacking direction because the typical π-π stacking spacing of 3.57 Å [18,19] did not made the two H atoms bond appropriately.

4. Conclusions

In summary, the catalysts composed of PDI assembly and Pd QDs with sizes of ∼5 nm were fabricated and displayed higher activities for visible-light photocatalytic degradation and hydrogen evolution than PDI/P25 owing to their "electron-storing" effect. The Pd QDs of PDI/Pd@P25 and Pd@PDI/P25 were distributed inside and outside the PDI

assembly, respectively. The photogenerated electrons in the PDI assembly transferred rapidly from PDI assembly to Pd QDs with the help of PDI radical anions, resulting in charge separation. Importantly, we disclosed a new electron transfer mechanism between the plasma metal and the self-assembly. In the system, hot electrons accumulated in the Pd QDs enhanced the Pd plasmonic oscillation and thus caused energy transfer and back-ET into the PDI assembly. Hence, an increasing population of the PDI radical anions was formed to enhance the reduction capability of the PDI assembly. The photocatalytic molecular mechanism demonstrated the transformation of the surface-bound O$_2$ into highly active h−O−O$^-$ and the electron hopping to H$^+$ which was adsorbed by C=O of PDI occurred to produce H$_2$. Moreover, the reaction sites on PDI were confirmed by the analysis of charge distribution and orbital overlap. It is anticipated that our work will result in new methods of designing a novel photocatalyst based on self-assembled supramolecular structure for potential energy preparation.

Appendix A. Supplementary data

Supplementary material related to this article can be found, in the online version, at doi:https://doi.org/10.1016/j.apcatb.2018.02.032.

References

[1] Y. Zhong, M.T. Trinh, R. Chen, W. Wang, P.P. Khlyabich, B. Kumar, Q. Xu, C.Y. Nam, M.Y. Sfeir, C. Black, M.L. Steigerwald, Y.L. Loo, S. Xiao, F. Ng, X.Y. Zhu, C. Nuckolls, J. Am. Chem. Soc. 136 (2014) 15215–15221.
[2] M. Sytnyk, E.D. Glowacki, S. Yakunin, G. Voss, W. Schofberger, D. Kriegner, J. Stangl, R. Trotta, C. Gollner, S. Tollabimazraehno, G. Romanazzi, Z. Bozkurt, M. Havlicek, N.S. Sariciftci, W. Heiss, J. Am. Chem. Soc. 136 (2014) 16522–16532.
[3] J. Mei, Y. Diao, A.L. Appleton, L. Fang, Z. Bao, J. Am. Chem. Soc. 135 (2013) 6724–6746.

[4] Y.H. Chen, D.G. Ma, J. Mater. Chem. 22 (2012) 18718–18734.
[5] L. Li, P. Gao, M. Baumgarten, K. Mullen, N. Lu, H. Fuchs, L. Chi, Adv. Mater. 25 (2013) 3419–3425.
[6] D. Liu, J. Wang, X. Bai, R. Zong, Y. Zhu, Adv. Mater. 28 (2016) 7284–7290.
[7] J. Wang, W. Shi, D. Liu, Z.J. Zhang, Y.F. Zhu, D. Wang, Appl. Catal.B 202 (2017) 289–297.
[8] N. Vallavoju, J. Sivaguru, Chem. Soc. Rev. 43 (2014) 4084–4101.
[9] A.S. Weingarten, R.V. Kazantsev, L.C. Palmer, D.J. Fairfield, A.R. Koltonow, S.I. Stupp, J. Am. Chem. Soc. 137 (2015) 15241–15246.
[10] A.S. Weingarten, R.V. Kazantsev, L.C. Palmer, M. McClendon, A.R. Koltonow, A.P. Samuel, D.J. Kiebala, M.R. Wasielewski, S.I. Stupp, Nat. Chem. 6 (2014) 964–970.
[11] M. de Torres, R. van Hameren, R.J. Nolte, A.E. Rowan, J.A. Elemans, Chem. Commun. (Camb.) 49 (2013) 10787–10789.
[12] L. Zeng, T. Liu, C. He, D. Shi, F. Zhang, C. Duan, J. Am. Chem. Soc. 138 (2016) 3958–3961.
[13] L.F. Dossel, V. Kamm, I.A. Howard, F. Laquai, W. Pisula, X. Feng, C. Li, M. Takase, T. Kudernac, S. De Feyter, K. Mullen, J. Am. Chem. Soc. 134 (2012) 5876–5886.
[14] Y. Che, H. Huang, M. Xu, C. Zhang, B.R. Bunes, X. Yang, L. Zang, J. Am. Chem. Soc. 133 (2011) 1087–1091.
[15] W. Che, W. Cheng, T. Yao, F. Tang, W. Liu, H. Su, Y. Huang, Q. Liu, J. Liu, F. Hu, Z. Pan, Z. Sun, S. Wei, J. Am. Chem. Soc. 139 (2017) 3021–3026.
[16] M.S. Rodriguez-Morgade, M.E. Plonska-Brzezinska, A.J. Athans, E. Carbonell, G. de Miguel, D.M. Guldi, L. Echegoyen, T. Torres, J. Am. Chem. Soc. 131 (2009) 10484–10496.
[17] W. Wei, D. Liu, Z. Wei, Y. Zhu, ACS Catal. 7 (2017) 652–663.
[18] K. Balakrishnan, A. Datar, R. Oitker, H. Chen, J. Zuo, L. Zang, J. Am. Chem. Soc. 127 (2005) 10496–10497.
[19] Y. Che, A. Datar, K. Balakrishnan, L. Zang, J. Am. Chem. Soc. 129 (2007) 7234–7235.
[20] F. Wurthner, Chem. Commun. (Camb.) (2004) 1564–1579.
[21] S.S. Li, H. Zhang, W.C. Zhao, L. Ye, H.F. Yao, B. Yang, S.Q. Zhang, J.H. Hou, Adv. Energy Mater. 6 (2016) 1501991.
[22] N.N. Liang, K. Sun, Z. Zheng, H.F. Yao, G.P. Gao, X.Y. Meng, Z.H. Wang, W. Ma, J.H. Hou, Adv. Energy Mater. 6 (2016) 1600060.
[23] I. Ghosh, T. Ghosh, J.I. Bardagi, B. Konig, Science 346 (2014) 725–728.
[24] C.J. Huber, S.M. Egger, I.C. Spector, A.R. Juelfs, C.L. Haynes, A.M. Massari, J. Phys. Chem. C 119 (2015) 25135–25144.
[25] Y.W. Su, W.H. Lin, Y.J. Hsu, K.H. Wei, Small 10 (2014) 4427–4442.
[26] D. Gosztola, M.P. Niemczyk, W. Svec, A.S. Lukas, M.R. Wasielewski, J. Phys. Chem. A 104 (2000) 6545–6551.
[27] Y. Che, A. Datar, X. Yang, T. Naddo, J. Zhao, L. Zang, J. Am. Chem. Soc. 129 (2007) 6354–6355.
[28] X. Chen, S. Shen, L. Guo, S.S. Mao, Chem. Rev. 110 (2010) 6503–6570.
[29] Q. Li, Y.W. Li, P. Wu, R. Xie, J.K. Shang, Adv. Mater. 20 (2008) 3717–3723.
[30] V. Suresh, D.Y. Kusuma, P.S. Lee, F.L. Yap, M.P. Srinivasan, S. Krishnamoorthy, ACS Appl. Mater. Interfaces 7 (2015) 279–286.
[31] T. Hirakawa, P.V. Kamat, Langmuir 20 (2004) 5645–5647.
[32] Y. Chen, A. Li, X. Yue, L.N. Wang, Z.H. Huang, F. Kang, A.A. Volinsky, Nanoscale 8 (2016) 13228–13235.
[33] S. Chen, Y. Li, C. Wang, RSC Adv. 5 (2015) 15880–15885.
[34] S. Chen, D.L. Jacobs, J.K. Xu, Y.X. Li, C.Y. Wang, L. Zang, RSC Adv. 4 (2014)

[35] 48486–48491.
[35] T. Sun, J. Song, J. Jia, X. Li, X. Sun, Nano Energy 26 (2016) 83–89.
[36] M. Ye, J. Gong, Y. Lai, C. Lin, Z. Lin, J. Am. Chem. Soc. 134 (2012) 15720–15723.
[37] J.M. Sanz, D. Ortiz, R.A. de la Osa, J.M. Saiz, F. Gonzalez, A.S. Brown, M. Losurdo, H.O. Everitt, F. Moreno, J. Phys. Chem. C 117 (2013) 19606–19615.
[38] T. Murahashi, T. Uemura, H. Kurosawa, J. Am. Chem. Soc. 125 (2003) 8436–8437.
[39] J. Cao, J.Z. Sun, J. Hong, X.G. Yang, H.Z. Chen, M. Wang, Appl. Phys. Lett. 83 (2003) 1896–1898.
[40] T. Schmidt, R.Q. Albuquerque, R. Kempe, S. Kuemmel, Phys. Chem. Chem. Phys. 124 (2016) 31966–31972.
[41] L. Jing, X. Sun, J. Shang, W. Cai, Z. Xu, Y. Du, H. Fu, Sol. Energy Mater. Sol. Cells 79 (2003) 133–151.
[42] L. Zang, Acc. Chem. Res. 48 (2015) 2705–2714.
[43] L. Zang, Y. Che, J.S. Moore, Acc. Chem. Res. 41 (2008) 1596–1608.
[44] K. Balakrishnan, A. Datar, R. Oitker, H. Chen, J. Zuo, L. Zang, J. Am. Chem. Soc. 127 (2005) 10496–10497.
[45] K. Balakrishnan, A. Datar, K. Balakrishnan, L. Zang, J. Am. Chem. Soc. 129 (2007) 7234–7235.
[46] M.V. Fedin, E.G. Bagryanskaya, H. Matsuoka, S. Yamauchi, S.L. Veber, K.Y. Maryunina, E.V. Tretyakov, V.I. Ovcharenko, R.Z. Sagdeev, J. Am. Chem. Soc. 134 (2012) 16319–16326.
[47] Z. Wang, W. Ma, C. Chen, H. Ji, J. Zhao, Chem. Eng. J. 170 (2011) 353–362.
[48] M. Sathiya, J.B. Leriche, E. Salager, D. Gourier, J.M. Tarascon, H. Vezin, Nat. Commun. 6 (2015) 6276.
[49] T. Nagamori, K. Marumoto, Adv. Mater. 25 (2013) 2362–2367.
[50] S. Sanshiro, O. Kazunari, J. Phys. Soc. Jpn. 65 (1996) 4062–4066.
[51] Q. Li, Y.W. Li, P. Wu, R. Xie, J.K. Shang, Adv. Mater. 20 (2008) 3717–3723.
[52] H. Hirakawa, S. Shiota, Y. Shiraishi, H. Sakamoto, S. Ichikawa, T. Hirai, ACS Catal. 6 (2016) 4976–4982.
[53] H. Li, F. Qin, Z. Yang, X. Cui, J. Wang, L. Zhang, J. Am. Chem. Soc. 139 (2017) 3513–3521.
[54] Y. Xiong, Y. Xia, Adv. Mater. 19 (2007) 3385–3391.
[55] G. Liu, P. Li, G. Zhao, X. Wang, J. Kong, H. Liu, H. Zhang, K. Chang, X. Meng, T. Kako, J. Ye, J. Am. Chem. Soc. 38 (2016) 9128–9136.
[56] L. Zeng, T. Liu, C. He, D. Shi, F. Zhang, C. Duan, J. Am. Chem. Soc. 138 (2016) 3958–3961.
[57] C. Tang, H.S. Wang, H.F. Wang, Q. Zhang, G.L. Tian, J.Q. Nie, F. Wei, Adv. Mater. 27 (2015) 4516–4522.
[58] H. Li, F. Qin, Z. Yang, X. Cui, J. Wang, L. Zhang, J. Am. Chem. Soc. 139 (2017) 3513–3521.
[59] M.C. Delgado, E.G. Kim, D.A. da Silva Filho, J.L. Bredas, J. Am. Chem. Soc. 132 (2010) 3375–3387.
[60] R.I. Bickley, R.K.M. Jayanty, Faraday Discussions of the Chemical Society vol. 58, (1974), pp. 194–204.
[61] L. Wang, Y. Wan, Y. Ding, S. Wu, Y. Zhang, X. Zhang, G. Zhang, Y. Xiong, X. Wu, J. Yang, H. Xu, Adv. Mater. 29 (2017) 1702428, http://dx.doi.org/10.1002/adma.201702428.
[62] Q.J. Song, T. Niu, H.J. Wang, J. Mol. Struc.-Theochem 861 (2008) 27–32.
[63] Jon M. Matxain, M. Ristila, Ake Strid, Leif A. Eriksson, Chem. Eur. J. 13 (2007) 4636–4642.
[64] R. Venkatadri, R.W. Peters, Hazard. Waste Hazard. Mater. 10 (2009) 107–149.